This document is the accepted manuscript version of the following article:
Pan, J., Durand, M. T., Courville, Z., Vander Jagt, B. J., Molotch, N. P., Margulis, S. A.,… Mätzler, C. (2021). Evaluation of stereology for snow microstructure measurement and microwave emission modeling: a case study. International Journal of Digital Earth. https://doi.org/10.1080/17538947.2021.1902006

Evaluation of stereology for snow microstructure measurement and microwave emission modelling: A case study

Jinmei Pan[a,b*], M. T. Durand[b], Z. Courville[c], B. J. Vander Jagt[b], N. P. Molotch[d], S. A. Margulis[e], E. J. Kim[f,] M. Schneebeli[g], C. Mätzler[h]

[a]State Key Laboratory of Remote Sensing Science, Aerospace Information Research Institute, Chinese Academy of Sciences, Beijing, China; [b]School of Earth Science and Byrd Polar Research Center, The Ohio State University, Columbus, OH, USA; [c]US Army Corps of Engineers Cold Regions Research and Engineering Laboratory, Hanover, NH, USA; [d]University of Colorado, Geography Department and Institute of Arctic and Alpine Research, Boulder, CO, USA; [e]Department of Civil and Environmental Engineering, University of California, Los Angeles, CA, USA; [f]Hydrospheric and Biospheric Sciences Laboratory, NASA Goddard Space Flight Center, Greenbelt, MD, USA; [g]WSL Institute for Snow and Avalanche Research SLF, Davos Dorf, Switzerland; [h]Institute of Applied Physics and Oeschger Centre for Climate Change Research, University of Bern, Bern, Switzerland

*Corresponding author: Jinmei Pan (panjm@aircas.ac.cn)

Abstract

Reliable microstructure measurement of snow is a requirement for microwave radiative transfer model validation. Snow specific surface area (SSA) can be measured using stereological methods, in which snow samples are cast in the field and photographed in the laboratory. Processing stereology photographs manually by counting intersections of test cycloids with air-ice boundaries reduces the problems in binary segmentation. This paper is a case study to evaluate the repeatability of the manually stereology interpretation by two independent research groups. We further assessed how uncertainty in snow SSA influences simulated brightness temperature (T_B) driven by the Microwave Emission Model of Layered Snowpacks (MEMLS), and how stereology compares to Near Infrared (NIR) camera and hand lens. Data was obtained from two alpine snow profiles from Steamboat Springs, Colorado. Results showed that stereological SSA values measured by two groups are highly consistent, and the ground radiometer measured T_B at 19 and 37 GHz was successfully predicted (RMSE<3.8K); simulations using NIR SSA and hand-lens geometric grain size (D_g) measurements have larger errors. This conclusion was not sensitive to uncertainty in the free parameters of T_B modelling.

Keywords: microwave radiometry; snow; stereology; snow microstructure; MEMLS

1. Introduction

Snow microstructure plays a critical role in snow hydrology and snow remote sensing; thus, methods to quantify snow microstructure in the field are of great importance. Snow microstructure governs many important snow physical properties such as thermal conductivity (Sturm et al., 1997), and radiative transfer properties for visible, near-infrared, and microwave wavelengths (Wiscombe & Warren, 1980; Mätzler, 1987). Snow microstructure is central to microwave remote sensing methods to estimate snow water equivalent (SWE) (Chang et al., 1987; Kelly, 2009). Rott et al. (2013) and Rutter et al. (2019) discuss the importance of an accurate snow microstructure estimate to constrain the SWE retrieval from Ku-band radar, a leading candidate for proposed snow

missions by multiple space agencies (Xiong et al., 2016; Derksen et al., 2019). Thus, objective, repeatable methods to measure snow microstructure in the field are critical.

The most traditional way to describe the snow microstructure is to use the geometric grain size (D_g), defined as the maximum extent of the prevailing grains (Fierz et al. 2009). D_g can be measured in the field using a ruled card and a loupe-style hand lens (Elder et al., 2009), or postprocessed from photos of dispersed snow grains on a ruled card (Lemmetyinen et al., 2016; Langlois et al., 2010). D_g measurement can still be subjective; in most cases, the natural snow structure is bonded. This structure must be disaggregated in the D_g measurement protocol, which may confound observer interpretation of particle dimension. In contrast, the snow specific surface area (SSA) metric begins with the assumption of a continuous snow medium, including both grains and bonds. Snow casts allow preservation of snow microstructure by displacing air space inside a snow sample with a suitable casting agent (see Section 4.3 for more details). Casts may be analyzed using either micro-Computed Tomography (CT; Pinzer et al., 2009; Ebner et al., 2015; Hagenmuller et al., 2016), or stereology (Davis & Dozier, 1989; Wiesmann et al., 1998; Reber et al., 1987; Matzl & Schneebeli, 2010; Riche et al., 2012) methods in the laboratory. Both approaches in principle allow for measurement of snow SSA and other microstructure properties directly, such as the density, two-point spatial auto-correlation function (ACF) and correlation length (L_c). The snow SSA can also be measured in the field using NIR photography (Matzl et al., 2006), contact spectroscopy (Painter et al., 2007), Shortwave Infrared (SWIR) integrating sphere (Gallet et al., 2009; Montpetit et al., 2012; Zuanon, 2013; Gergely et al., 2014) and Snow Micro-Penetrometer (SMP) (Proksch et al., 2015a), but these approaches generally require validation using laboratory methods applied to “snow casts”. The basis of the micro-CT is identical to medical x-ray CT: the sample is

74 illuminated by x-rays, the transmitted signal is measured, and the interior structure of
75 the sample is numerically reconstructed, in the form of a three-dimensional map of ice-
76 air classification. While the CT approach has been widely used in recent years (Avanzi
77 et al., 2017; Wiese & Schneebeli, 2017; Ishimoto et al., 2018; Eppanapelli et al., 2019),
78 a CT machine is expensive, and CT analysis includes specification of a threshold used
79 to perform the ice-air segmentation (Hagenmuller et al., 2016). In contrast to the CT
80 approach, stereology is based on photographed surface sections of snow sample. The
81 stereology approach requires only a cold laboratory, a microtome and a camera, and is
82 thus significantly more accessible than CT.

83 There are two approaches to stereology: one in which each pixel in the snow
84 sample photographs is classified into ice or air, and one in which images are interpreted
85 manually. The process of classifying each pixel into ice or casting agent is called the
86 segmentation. A successful segmentation requires samples with only few air-bubbles
87 and little recrystallization of casting agent (Matzl & Schneebeli, 2010); otherwise, using
88 a fixed threshold to do the classification will introduce errors. Indeed, threshold-
89 determining methods like sequential filtering and energy-based approaches in
90 Hagenmuller et al. (2016) essentially require a bi-modal histogram of pixel values. In
91 contrast, manual interpretation of stereology images can be done far more accurately. It
92 is regularly held for stereology applications in general (i.e. mostly outside of snow) that
93 manual interpretation is more reliable than automated segmentation (Shain et al., 1999;
94 Haass-Koffler et al., 2012; Phoulady et al., 2019). Even for images of samples that show
95 casting agent recrystallization, the snow SSA can be measured by manually counting
96 the intersections of a test system of cycloid lines overlaid on the photograph with the
97 ice-air interfaces (Riche et al., 2012). However, the repeatability of this approach for

98 measuring snow SSA across different observers needs to be examined, which is the
99 focus of this paper.

100 In this paper, the stereological method to measure snow SSA based on manually
101 counting protocol was tested over a deep alpine snow at Steamboat, Colorado, US in
102 2010. The stereological photos were interpreted by two independent research groups,
103 and the difference in measured snow SSA and how the difference propagates in the
104 passive microwave brightness temperature (T_B) simulation were evaluated. Direct snow
105 microstructure measurement is the key to support the physically-based remote sensing
106 model simulations (Xiong et al., 2012; Malinka, 2014), clarify complex relationships
107 between different snow microstructure parameters (Löwe et al., 2015; Chang et al.,
108 2016) and reinforce the understanding of newly-observed snow signal characteristics
109 (Leinss et al., 2016).

110 In this study, the snow microstructure was also measured by hand lens and a
111 NIR camera to be compared with the stereology. We are interested in the performance
112 of different methods to describe the small and large snow particle dimensions, and how
113 the errors comprehensively influence the T_B of a deep natural snowpack of vertically
114 inhomogeneity. The snow T_B was observed by a ground-based radiometer at 19 and 37
115 GHz, vertical polarization, at an incidence angle of 50°. The Microwave Emission
116 Model of Layered Snowpacks (MEMLS) based on Improved Born Approximation (IBA)
117 (Mätzler, 1998; Mätzler & Wiesmann, 1999) is used as the modelling tool. The
118 microstructure assumption of MEMLS-IBA is compatible with SSA. The
119 microstructure parameters measured by stereology, NIR photography and hand lens
120 were converted to the exponential correlation length (L_e) required by MEMLS using
121 both the conventional coefficients from previous literatures and the optimized

coefficients. We will further discuss the influence of soil parameters to modelling results.

2. Snow microstructure based on continuous snow medium assumption

There are several parameters that can be used to describe a continuous snow medium, including the surface areas, curvatures, chord length distributions, correlation lengths and two-point spatial Auto Correlation Functions (ACF) (Mätzler, 2002; Krol & Löwe, 2016). Surface area of snow refers to the area of ice-air interface. Correlation lengths are highly relevant to ACF. The later evaluates the correlation of two random points in the medium as a function of the displacement between these two points. Taking the dry snow medium as an example, the two points will be considered of high correlation if they are both occupied by ice or air pore, and will be considered of low correlation if one is occupied by ice and the other is occupied by air. ACF is from the statistics of multiple pairs of points in the medium. An equation to calculate ACF for dry snow can be found in Mätzler (1997).

The snow specific surface area (SSA) is usually defined as the ratio of the total surface area of ice (including grains, bonds, etc.) (unit: m^2) to the total volume (unit: m^3) or total mass (unit: kg) of ice. SSA in the former case is denoted as S_i (unit: m^{-1}) in our paper. The surface to volume ratio, S/V (unit: m^{-1}), represents the ratio of the total surface area of ice to the total volume of snow. S/V is related to S_i as:

$$S/V = S_i \times v \tag{1}$$

where, v (unitless) is the ice volume fraction, calculated by snow density divided by ice density.

In Debye et al. (1957), it theoretically deducted the relationship between S/V and the derivative of two-point spatial Auto Correlation Functions (ACF) at zero

displacement, and Mätzler (2002) utilized this derivative to define a parameter called the correlation function (L_c) as follows:

$$L_c = -\left(\frac{dA(x)}{x}\right)^{-1}\Big|_{x=0} = \frac{4v(1-v)}{S/V} \quad (2)$$

where, $A(x)$ is ACF. L_c is in mm.

A fit to ACF by an exponential function gives the exponential correlation length (L_e) (Mätzler, 2002) which follows:

$$A(x) = e^{-\frac{x}{L_e}} \quad (3)$$

If the snow ACF strictly follows an exponential-shape curve, L_e equals L_c. However, it has been found by Mätzler (2002) and Krol and Löwe (2016) that, for natural snow samples, L_e and L_c can have different values when the slope of ACF is steeper or more flat near the origin. The reason is L_e fitted by ACF over the full domain represents a longer-range autocorrelation, whereas L_c determined near the origin is from autocorrelation over very short length scales. In this case, a scaling factor is required to convert L_c to L_e as shown below:

$$L_e = \beta L_c \quad (4)$$

Substituting equation (4) into equation (1) and (2) gives a conversion from *S/V* and S_i to L_e as:

$$L_e = \beta\frac{4v(1-v)}{S/V} = \beta\frac{4(1-v)}{S_i} \quad (5)$$

Using the measurement of snow samples from Weissfluhjoch, Davos, Switzerland by stereology, Mätzler (2002) found a mean value of β as 0.75, with a standard deviation of 0.15. For different samples, β varies from about 1.0 for depth hoar to 0.66 in average for fresh snow. From the recent experiment in Krol & Löwe (2016), the average β is 0.79, and they explained the difference is from the more depth hoar

samples included. Krol & Löwe (2016) also found a second-order ACF parameter called the curvature length can be used to narrow down the uncertainty in β estimate. Then, β can potentially be linked to a measurable objective parameter instead of the grain shape classification.

3. Microwave Emission Model for Layered Snowpack (MEMLS)

3.1 Model introduction

A seasonal snowpack is fundamentally a layered medium (Colbeck, 1991). In many cases, the snow microwave emission cannot be understood without the layered characteristics of snowpacks (Hall et al., 1986; Boyarskii & Tikhonov, 2000; Durand et al., 2011). This has motivated the development of multi-layer radiative transfer models. In this study, we utilize the Microwave Emission Model of Layered Snowpacks (MEMLS) (Wiesmann & Mätzler, 1999), one of the first multi-layer snow RT models established from extensive theoretical (Mätzler, 1997; Mätzler, 1998; Mätzler & Wiesmann, 1999) and experimental (Wiesmann et al., 1998; Mätzler, 2002) studies. The Improved Born Approximation (IBA) was used to calculate the MEMLS scattering coefficient, for its stronger physical basis and outstanding unbiased performance at different frequencies compared to the empirical MEMLS scattering coefficient (Pan et al., 2016).

MEMLS treats snow as a continuous medium composed of ice and air. To simplify the requirement for inputs, it assumes the snow ACF follows an exponential function as in equation (3). MEMLS requires L_e, whereas the stereology provides S/V, NIR camera provides S_i and hand lens provides D_g. A conversion of these microstructure parameters is needed, and will be described as follows.

3.2 MEMLS driven by SSA measurements

The snow SSA measurements have been widely used to drive the radiative transfer (RT) models for the passive microwave brightness temperature (T_B) simulation (Brucker et al., 2011; Rutter et al., 2014; Roy et al., 2013; Proksch et al., 2015b; Sandells et al., 2017). The accuracy of the snow radiative transfer (RT) models is expected to be higher when the snow microstructure assumptions between the model and the measurement are closer. Commonly, a scaling factor is needed when the two assumptions diverge, like the difference between L_e and L_c in Mätzler (2002) and the difference between optical grain size from SSA and the diameter of identical ice spheres in DMRT-ML (Dense Media Radiative Transfer – Multi Layer model) (Picard et al., 2013) in Roy et al. (2013). Hereafter, the β value of 0.75, derived from the direct snow microstructure measurement, is mentioned as β_M, and will be considered as a literature-based reference value to support the conversions in equation (5).

When β was derived from the optimization of T_B simulations, it was found to have larger variation range (Montpeitit et al., 2013; Brucker et al., 2011), with the possibility being to compensate for errors from other sources. Montpeitit et al. (2013) used a β of 1.3 for snow in Canada. Brucker et al. (2011) used a β of 2.08 for snow in Antarctica. Likewise, we also calculated an optimized β (called β_O hereafter) for our case.

3.3 MEMLS driven by geometric snow grain size measurements

To support the use of legacy D_g measurements, the empirical relationship between D_g and S was studied (Mätzler, 2002; Langlois et al., 2010). It has been checked in Durand et al. (2008), Pan et al. (2016) and Montpetit et al. (2013) that MEMLS can be driven by D_g measurements with a T_B RMSE of approximately 10 K.

Durand et al. (2008) developed an empirical relationship based on the measurements in Mätzler (2002) as:

$$L_e = \begin{cases} a_0 + a_1 lnD_g & (v > v_0 \; and \; D_g > D_{g0}) \\ L_{e0} & (otherwise) \end{cases} \quad (6)$$

Where, a_0=0.18 mm, a_1=0.09 mm, which were best-fit parameters for a logarithmic relationship between D_g and L_e. v_0=0.2, D_{g0}=0.125 mm, L_{e0}=0.05 mm, which were used to determine a fixed threshold L_e for low density, small grain size snow.

However, for the snow in Sodankylä, Finland, Pan et al. (2016) refitted a new set of coefficients as a_0=0.23 mm and a_1=0.13 mm from the fast SSA measurements, which gives higher T_B simulation performance compared to the Durand et al. (2008)'s coefficients. Interestingly, the ratios of a_0 and a_1 between Pan et al. (2016) and Durand et al. (2008) are close, with an average value of 1.36. Neglecting the slight shape difference, we added an optimized multiplication scaling factor, α, to equation (6) as:

$$L_e = \alpha L_e^D(D_g) \quad (7)$$

where, $L_e^D(D_g)$ is the L_e estimated using Durand et al. (2008)'s coefficients. An α of 1.0 is denoted as α_D. The optimized α is denoted as α_O.

4. Data and methods

We collected concurrent ground-based radiometric and snowpit measurements in the yard of the Storm Peak Laboratory (SPL), located in the Rocky Mountains, Colorado, USA, at 40°27'18", -106°44' 38", 3220 m height above sea level. SPL is within the Rabbit Ears study area of the NASA Cold Lands Processes Experiment (CLPX) in 2002-2003 (Elder et al., 2009). The site is located at the top of a small mountain, in a fairly exposed area with high winds and low temperatures typical throughout the winter. Deep snowpacks commonly accumulate. The nearby SNOTEL snow pillow site "Tower" (06J29S) reports an average SWE of 95.5 cm on April 1 (from 1975 to 2010).

Our study period spanned three days, 21 to 23 February, 2010. From the nearby Tower SNOTEL site, there was no change in SWE (i.e. no precipitation). Within these three days, the daily maximum air temperature at Tower site (20 m lower than SPL) was -5 ~ -9.4 ℃, and the daily minimum air temperature was -19.4 ~ -15.5 ℃.

4.1 Radiometer data

In order to measure the snow microwave radiance, we used a ground-based version of the NASA Airborne Earth Science Microwave Imaging Radiometer (AESMIR) operating at 19 and 37 GHz (Kim, 2009). We mounted the radiometer approximately 3.5 meters vertically above the soil-snow interface, with an incidence angle of 50° up from nadir. The antennas have a narrow Full Width Half Maximum (FWHM) beamwidth of 8°, such that footprint has an area of approximately $\pi \times 0.12 \times 0.30$ m^2 on the snow surface and $\pi \times 0.24 \times 0.60$ m^2 on the soil surface.

Only the vertically-polarized T_B was measured. We performed a two-point calibration once per day. On each day, a snap-shot measurement between 30 ~ 60 minutes (warm-up and calibration time excluded) was conducted. All voltage measurements were integrated over thirty-second periods using a fast-sampling voltage meter. The measured average T_B at 19 GHz, vertical polarization is 247.5, 252 and 248 K from 21 to 23 February, respectively, and that at 37 GHz is 227, 233 and 231 K, respectively. We are confident in our T_B observations as the T_B values differed by only few K without new snowfalls when the radiometer was calibrated independently for each observation.

4.2 Snowpit data

The snowpits were excavated on 22 and 23 February near to the ground-based radiometer. The pit on 22 February was approximately two meters from the center of

265 the field of view (FOV), whereas the pit on 23 February was excavated directly in the
266 center of the radiometer FOV after the T_B measurement was made.

267 The wind-blown effect resulted in a slightly larger depth in the up-hill direction
268 and a small depth in the down-hill direction. Therefore, we observed different pit depths
269 of 174 cm and 165 cm on 22 and 23 February, respectively, with their SWE as 547 mm
270 and 497 mm. The snowpits were evacuated perpendicular to the contour to capture the
271 depth variability. As can be seen from the NIR photos in Figure 1 and 2, the landscape
272 and the wind-blown effect resulted in some slant sub-interfaces which are not parallel to
273 the ground. Therefore, the horizontal polarization was not explored to reduce the
274 impacts on MEMLS simulation.

275 Stratigraphy of each pit was identified using standard snow hardness tests based on
276 protocols established under the CLPX field campaign (Elder et al., 2009). There were
277 six layers identified on 22 February and eight layers identified on 23 February (see
278 Figure 3). Counted in the bottom-first order, layer 1 (the bottom layer) on both days was
279 identified as depth hoar, and layer 2 was identified as composed of facetted crystals.
280 These two bottom layers were followed by a few layers of faceted/round mix and
281 rounds, and the topmost two layers were identified as new snow composed of partly
282 decomposed precipitation particles. No ice lenses were found in both snowpits.

283 The geometric grain size (D_g) was measured using the aid of a loupe-style hand
284 lens; following the CLPX grain size measurement protocol. The maximum and
285 minimum dimensions of the large, medium and small snow grains were measured for
286 each stratigraphic layer. The maximum dimension of the medium snow grains is closest
287 to the definition of D_g in Mätzler (2002) and Fierz et al. (2009), written as the maximum
288 dimension of the prevailing grains. Profiles of the measured D_g can also be found in
289 Figure 3. It shows the measured D_g at the bottom of February 23 snowpit is much

290 smaller than expected, albeit a depth hoar snow type. The reason will be discussed in
291 Section 5.1. However, given the subjective nature of the D_g measurements, especially
292 those from a hand lens, this discrepancy is unsurprising. Snow temperature was
293 measured using a standard field thermometer to a precision of 1° C, at vertical
294 increments of 10 cm. Snow density was measured to a precision of 1 kg m^{-3} by a wedge
295 density cutter of 1000 cm^3 volume.

296

297

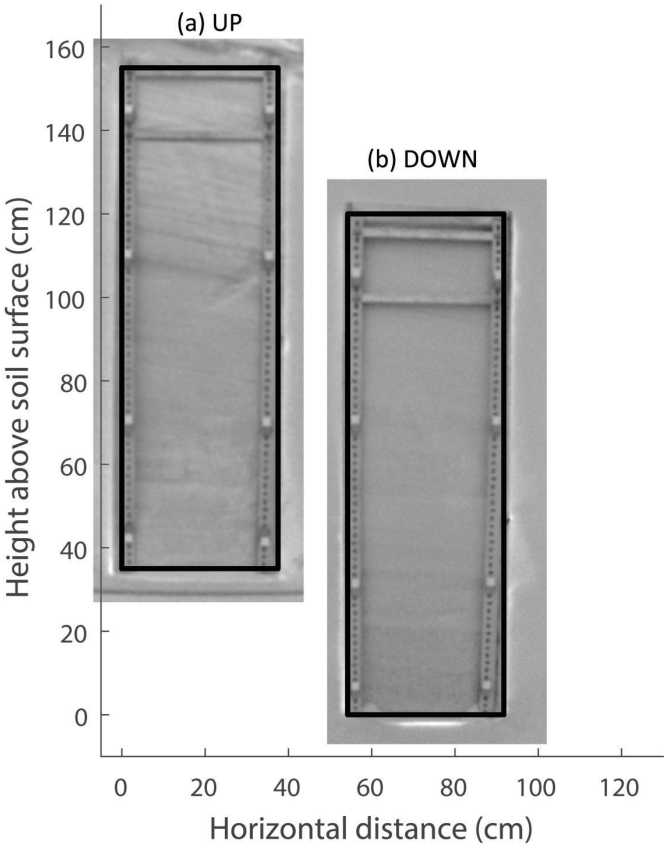

298

299 Figure 1. NIR photo of the snowpit on 22 February. The full snow profile was
300 photographed by two times. Firstly, a metal frame (37 cm × 120 cm size) was attached
301 to the upper portion (a) of the profile and pictured; later, it was moved to the lower
302 portion (b). Note that the topmost 12 cm was missed on this day when the snow was too
303 loose to hold the frame.

304

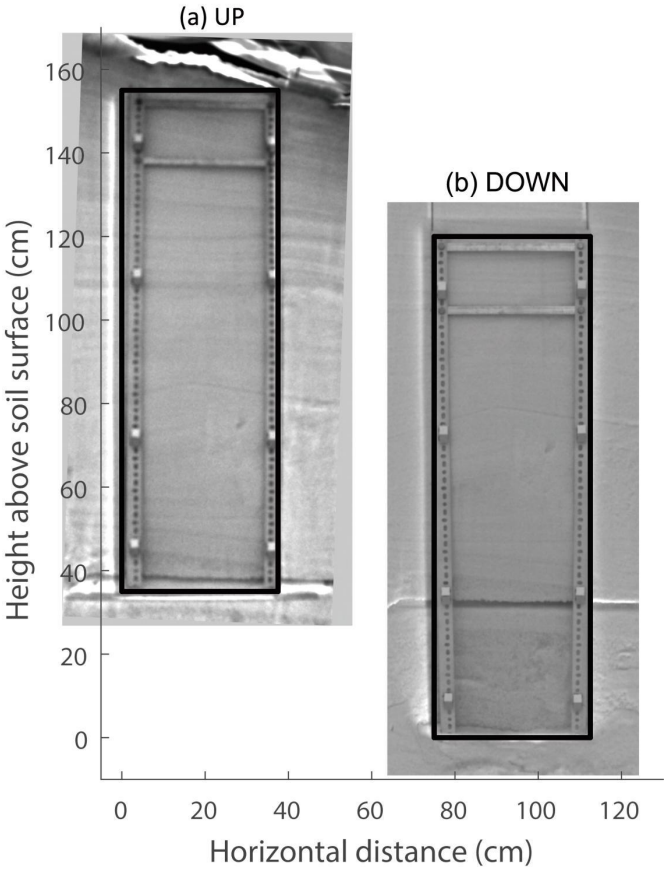

Figure 2. NIR photo of the snowpit on 23 February, photographed by the same method in Figure 1.

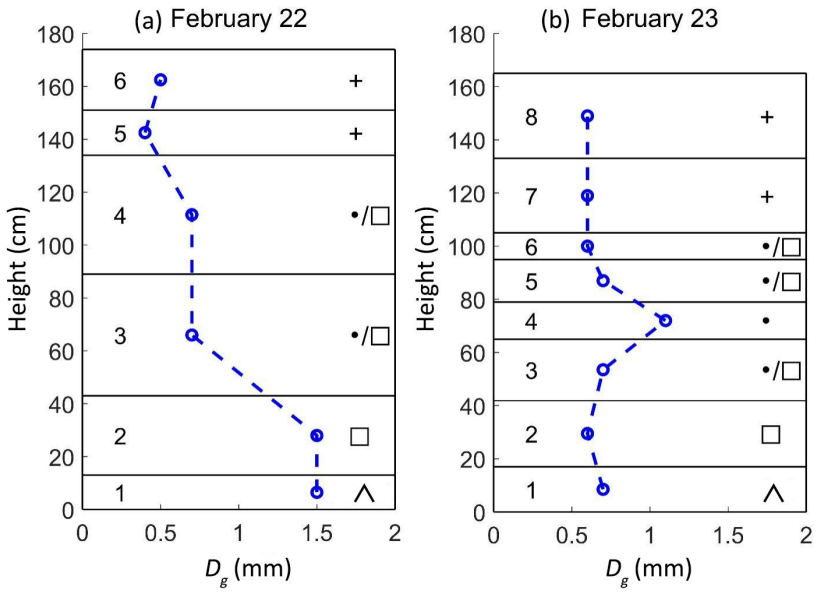

Figure 3. Stratigraphy, geometric grain size, and morphological classification according to Fierz et al. (2009) for the snowpits on 22 February (a) and 23 February (b).

4.3 Stereological analysis of snow samples

We made snow casts for stereological analysis. For each of the stratigraphic layers identified in the snowpit, a cubic sample of snow approximately 10 cm on each side was extracted. The vertical axis of each sample was noted on sample containers. We preserved the samples in the field using dimethyl phthalate dyed with Sudan black, following the procedure of Perla et al. (1986). In the laboratory, samples were maintained at cold temperature temperatures below the melting point of the dimethyl phthalate during processing. Only the innermost section (~20 mm × 8 mm × 8 mm) of each sample was analyzed, in order to minimize any effects of degradation near the edges. The sample was repeatedly cut (i.e. shaved back) by 1 mm step parallel to the vertical direction in the snowpit using a microtome, and photographed, twenty times. Cuts were made such that the sample face (8 mm ×8 mm) represents a vertical section defined in Riche et al.(2012). The ice and dimethyl phthalate dust was vacuumed with a shop vac attachment on the microtome to keep sample clean. Photographs were made

328 with a Canon EOS 60D 18 mpixel resolution camera with a Canon EF100 mm f/2.8 L
329 macro lens illuminated by a ring light. Two photographs were taken of each face, one
330 with a ruler of 1-mm grids overlaid in order to enable determining pixel size. Note that
331 the samples were not thin section, nor was the ice sublimated off.

332 Successful casts of layers 1-4 were made for 22 February, and successful casts
333 of layers 1-5 were made for 23 February. Casts of the topmost layers (layers 5-6
334 February 22, layers 6-8 on February 23) were unsuccessful, as revealed by inspection of
335 the snow section photographs. Therefore, L_e for these layers were estimated as follows.
336 For Layer 5 and 6 on February 22 and layer 8 on February 23, L_e was estimated to be
337 0.05 mm, a typical value for fresh snow, referring to L_{e0} in equation (5). For layer 6
338 and 7 on February 23, L_e was assumed to be identical to layer 4 on February 22 because
339 of similarity in D_g, density and height in the snowpit.

340 Figure 4 and Figure 5 show one photograph (out of 20 in total) from each
341 successfully-casted sample. Black pixels indicate ice, grey pixels indicate dimethyl
342 phthalate originally occupied by pore space, and white pixels indicate either
343 recrystallized dimethyl phthalate or air bubbles. Layer 1 on February 23 has some
344 special horizontally-oriented thin structures, which were not observed in any other
345 layers. This is from the side walls of connected, strongly striated, hollow depth hoar
346 crystals. It has an observable difference with Layer 1 on February 22.

347 In order to calculate S, we used the methods explained and described in Matzl
348 and Schneebeli (2010). The basic principle of the methodology is to overlay a test
349 system of cycloids (following $x = 2\theta - sin2\theta$, $y = 1 - cos2\theta$ for $0 \leq \theta \leq \pi/2$) on
350 each image: see Figure 6 as an example. An unbiased estimate of S/V can be retrieved
351 using:

352 $$S/V = \frac{2I}{d} \quad (8)$$

where, I is the number of intersections between the cycloids and the air-ice boundaries, and d is the cycloid length.

For validation purposes, the stereological counting was done by two separate research teams from Ohio State University (OSU) and Swiss Federal Institute for Forest, Snow and Landscape Research (WSL). The two groups overlaid the cycloids in different ways, but they both visually counted the intersections without doing binary segmentation. Ice volume fraction of the sample, v, in equation (5) was calculated as the fraction of randomly-placed test points identified as ice in the stereological image.

The differences in the counting protocols from two research groups are as follows. First, the raw stereological photos were resized to coarser resolution to smooth the noise. Factors including the computer screen and the subjectivity of the observer influence pixel size. Calculated using the 1-mm ruler, it turns out the pixel size from the OSU group was between 6.45 to 10.20 μm, whereas that from the WSL group was between 10.53 to 12.34 μm; both varied per photo. Second, the test system used by the OSU group includes 9 cycloids, and it used the two ends of cycloids (i.e., 18 test points) to calculate v. The WSL group used 25 cycloids to calculate S and 100 test points to calculate v. The cycloid length was ~12.13 mm (177 pixels) used by the OSU group, and ~7.66 mm (68 pixels) used by the WSL group.

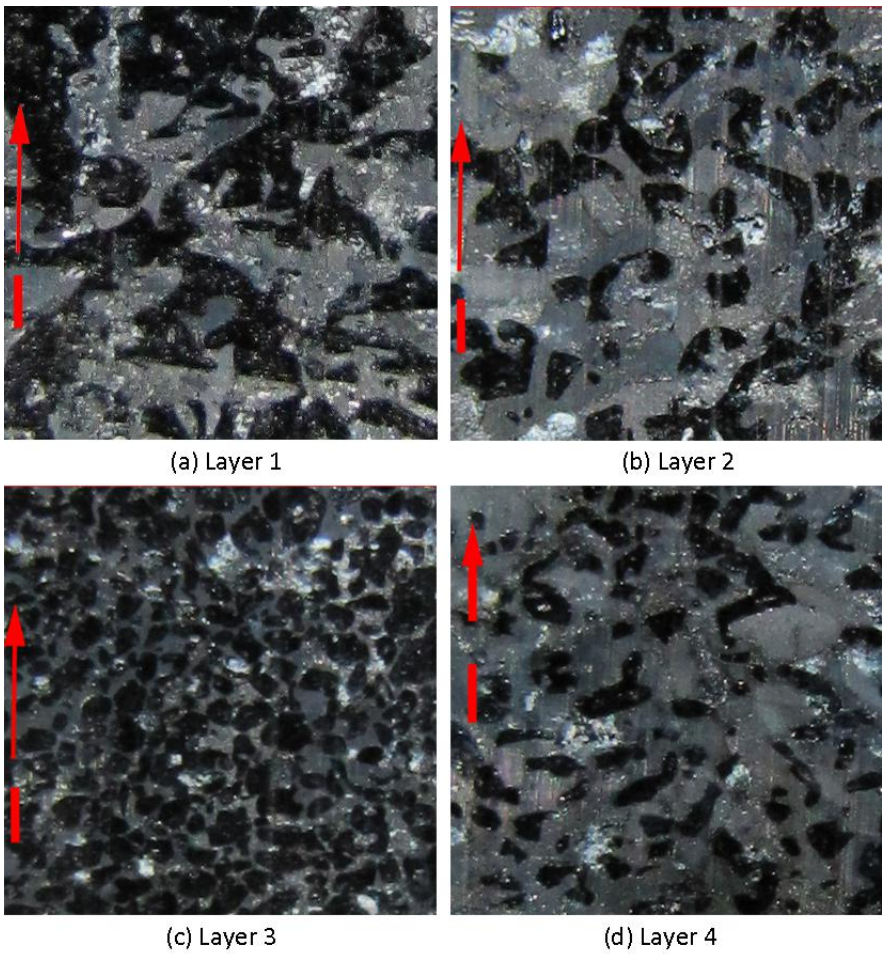

Figure 4. Stereological photographs of snow samples on February 22: (a) Layer 1 (depth hoar), (b) Layer 2 (facets), (c) Layer 3 (facets/round mix), (d) Layer 4 (facets/round mix). The vertical bar is a 1-mm ruler. The arrow indicates the upward direction in the snowpit.

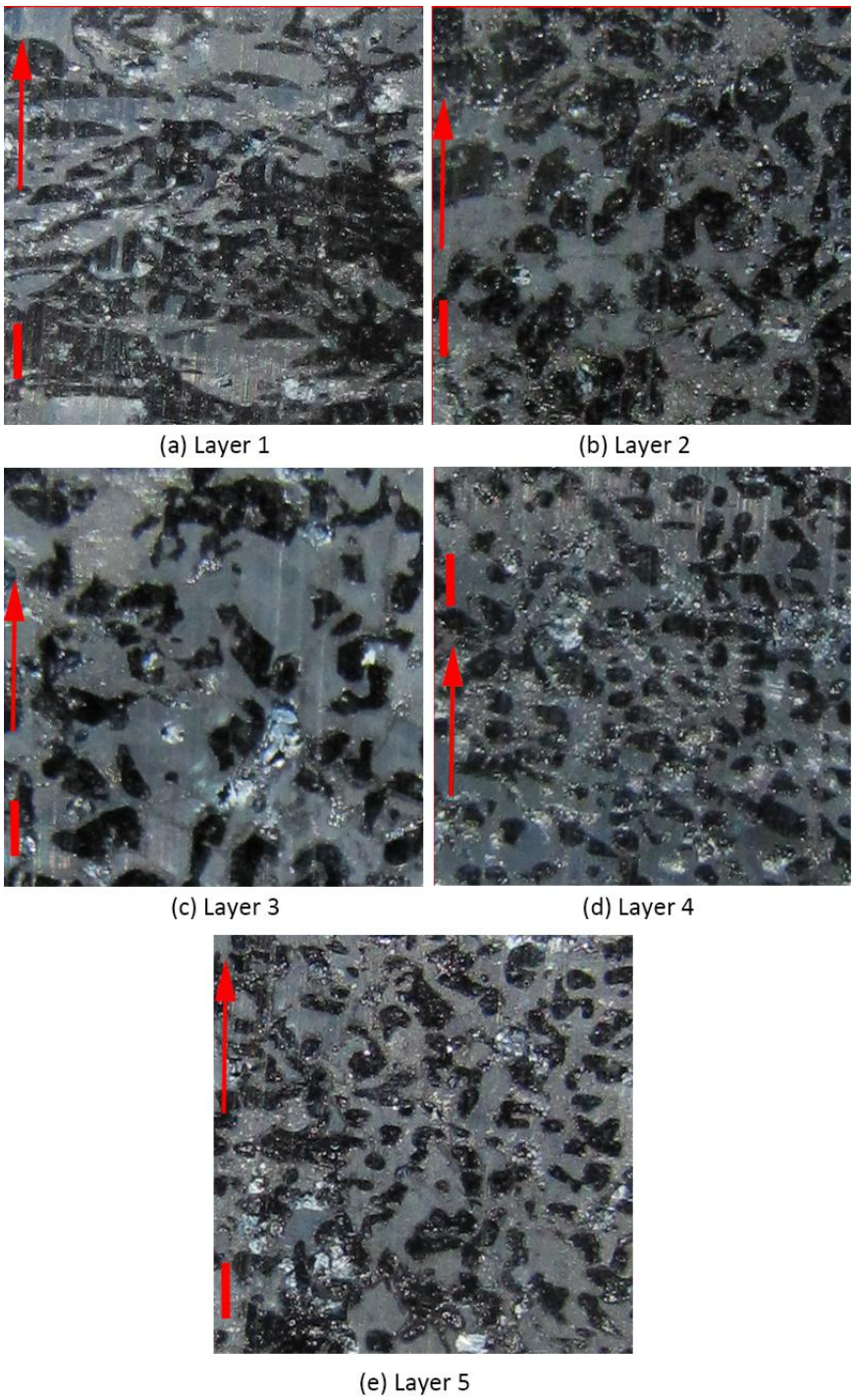

Figure 5. Stereological photographs of snow samples on February 23: (a) Layer 1 (depth hoar), (b) Layer 2 (facets), (c) Layer 3 (facets/round mix), (d) Layer 4 (rounds), (e) Layer 5 (facets/round mix).

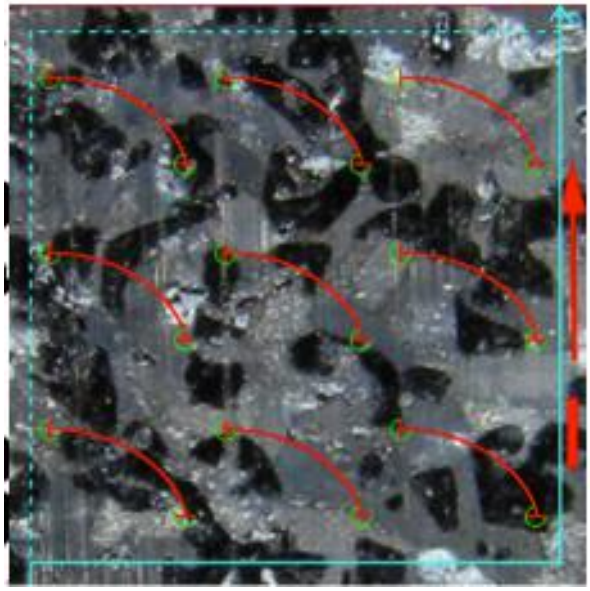

Figure 6. An example of cycloids overlaid on the stereological photo.

4.4 Near infrared analysis of snow samples

In the field, a vertical wall of the excavated snowpit was photographed by a NIR camera to deliver the spatial information of *S*, following the procedure of Matzl and Schneebeli (2006).

The camera used to take NIR photo was a Canon G14. The wavelength of the detected light ranged from 840 to 940 nm, which is exactly the same as the camera used in Matzl and Schneebeli (2006). The distance between camera and pit wall varied between 1.4 and 2.0 m, resulting in an area of pit wall from 0.5 to 1.0 m^2. The ~2 m depth snow pit wall was photographed by two parts (the upper and the lower part). See Figure 1 and Figure 2. A metal frame was used to provide geometrical information and to mount pairs of Spectralon calibration targets of 50% and 99% reflectance. A semitransparent tarp was used to cover the pit hole to reduce direct sunlight. A flat white foam covering the pit wall was also photographed to correct the illumination difference of diffuse light.

The NIR reflectance, *r*, of the snow was calibrated using:

$$r = a + bi \quad (9)$$

where, i is the illumination-corrected pixel intensity (digital numbers of pit wall photo divided by the white foam photo), and a and b are determined by a linear regression between i and the reflectance of calibration targets. Afterwards, S_i was calculated as (Matzl and Schneebeli, 2006):

$$S_i = Ae^{r/t} \quad (10)$$

where, r is in %; A and t are empirical constants as 0.017 mm^{-1} and 12.222, respectively.

The estimates of NIR S_i were averaged within each stratigraphic layer. The topmost part of the snow profile outside the metal frame (~ 12 cm on February 22, ~ 33 cm on February 23) was filled by the S_i right beneath that part, before processed to layer average. The v used to convert S_i to L_e was from snow cutter density measurements.

4.5 Optimization of conversion coefficients between snow microstructure parameters

As mentioned in the previous section, conversion coefficients are needed to convert S/V, S_i and D_g to L_e. Besides the literature-based conventional values, we calculated the optimized β_O and α_O using a cost function as:

$$f_c = \sqrt{\frac{(19v_M - 19v_O)^2_{Feb22} + (37v_M - 37v_O)^2_{Feb22} + (19v_M - 19v_O)^2_{Feb23} + (37v_M - 37v_O)^2_{Feb23}}{N}} \quad (11)$$

where, $19v_M$ and $19v_O$ are the predicted and observed T_B at 19 GHz, vertical polarization; $37v_M$ and $37v_O$ are defined similarly; N is the number of measurements, which is 4 in our case. f_c is also the root-mean squared error (RMSE) of predicted T_B for two frequencies, two snowpits.

To run MEMLS, the downwelling sky brightness temperature was set as 21 K and 33 K, respectively at 19 and 37 GHz, modelled by an 80% relative humidity under clear sky condition. The soil reflectivity was calculated by the Wegmüller and Mätzler (1999) model, using the bottom-most snow temperature as the physical temperature and a 0.1-cm soil roughness. The frozen soil dielectric constants were calculated using the Zhang et al. (2003) model. When Zhang et al. (2003) model was used, we used zero ice content and set the unfrozen volumetric soil water content (m_{vu}) was a free parameter. In the base simulation, a 12% m_{vu} was used, and later a sensitivity test was presented in Section 6.1.

5. Results

5.1 Comparison of snow microstructure measurements

Figure 7 shows the comparison of the measured *S/V* from stereological counting by the OSU and WSL groups. It shows the measured *S/V* from two research groups agreed with a mean relative difference of 2.7% and a root-mean squared error of 10%. The small difference from two research groups lends credence to the reliability of the stereological method. Table 1 and Table 2 list S_i and L_c converted from *S/V* for the snowpits on February 22 and 23, respectively. To convert *S/V* to L_c, we used a single set of v from the WSL group. This is because WSL used 100 test points, whereas OSU used only 18 test points, and we found this difference caused approximately 11% systematically larger v from OSU than WSL. Such bias was not found for the *S/V* measurements. After conversion, the mean relative difference of L_c is -1.8%, and the root-mean squared difference is 8.8%.

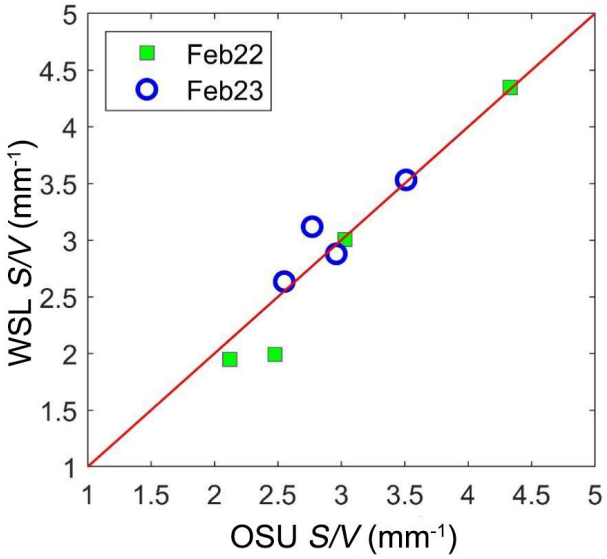

446

447 Figure 7. Comparison of measured *S/V* calculated from Ohio State University (OSU)
448 and Swiss Federal Institute for Forest, Snow and Landscape Research (WSL) groups.

449

450 Table 1. Stereology analysis for the snowpit on February 22.

Layer# In Bottom-first Order	Ice Volume Fraction, v	Surface to Volume Ratio, S/V (mm^{-1})		Specific Surface Area Per Ice Volume, S_i (mm^{-1})		Correlation Length, L_c (mm)	
		WSL	OSU	WSL	OSU	WSL	OSU
1	0.429	1.95	2.12	4.54	4.94	0.503	0.462
2	0.312	1.99	2.48	6.38	7.93	0.431	0.347
3	0.410	4.35	4.33	10.61	10.56	0.223	0.223
4	0.243	3.01	3.03	12.37	12.47	0.245	0.243

451

452 Table 2. Stereology analysis for the snowpit on February 23.

Layer# In Bottom-first Order	Ice Volume Fraction, v	Surface to Volume Ratio, S/V (mm^{-1})		Specific Surface Area Per Ice Volume, S_i (mm^{-1})		Correlation Length, L_c (mm)	
		WSL	OSU	WSL	OSU	WSL	OSU
1	0.370	3.12	2.77	8.42	7.48	0.299	0.337
2	0.394	2.88	2.96	7.31	7.51	0.332	0.323
3	0.284	2.63	2.55	9.27	8.98	0.309	0.319
4	0.359	3.53	3.51	9.85	9.79	0.261	0.262
5	0.311	N/A	3.73	N/A	12.00	N/A	0.230

453

Figure 8 shows the comparison of the layered L_e converted from stereological S/V and NIR S_i measurements using β_M (as 0.75) and from D_g measurements using α_D (as 1.0). It also includes the fine-resolution NIR profile. There is a crack (at ~ 37 cm height) observable on the February 23 pit wall from the NIR photo; thus the NIR data at this location was removed to reduce its influence on the L_e statistics. From Figure 8, first, it shows in general, the different estimates of L_e are well-correlated, with the exception of hand lens estimates for the bottom-most layer on February 22 and hand lens, stereological, and NIR estimates for the two bottom layers on February 23. Second, it shows the 0.05-mm L_e used for unsuccessfully-casted stereological samples at topmost layer is lower than the L_e estimates from NIR- and hand lens measurements. These assumed L_e for the stereological method may introduce errors to the T_B simulation, but we are also not confident on the other two methods, too. Third, for the bottom layer on February 23, some reasons for the differences can be found. As mentioned previously, the stereological counting was done independently by two different research groups. Therefore, we are confident in the stereological estimates. From the stereological photo in Figure 5(a), the special snow microstructure of Layer 1 on February 23 has a smaller dimension compared to that on February 22. It can result in the smaller D_g measured by hand lens and the larger S/V measured by stereology; in both cases, a smaller L_e is produced. However, comparison between the bottom part of NIR photos in Figure 1 and Figure 2 shows the crack and the rougher pit wall on February 23 can result in a decreased reflectance; in this case, a larger L_e is produced and diverges from the other two methods.

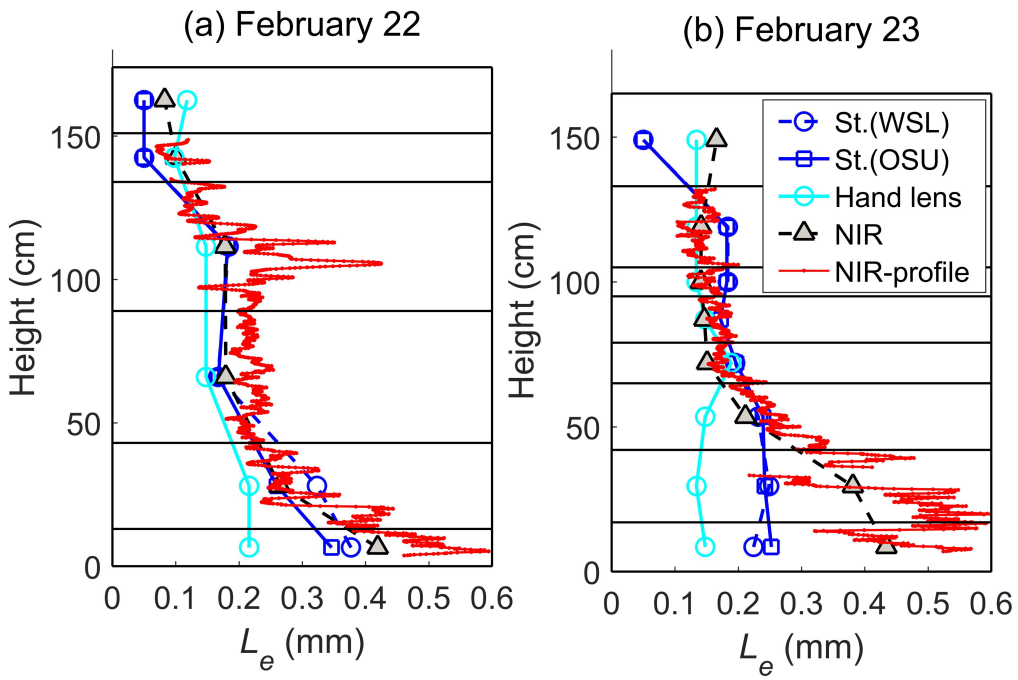

Figure 8. Profile of L_e using different measurement tools: (a) February 22, (b) February 23. St. represents stereology. For all methods, the conventional conversion coefficients are used.

5.2 Brightness temperature simulations

Figure 9 shows the error of the predicted T_B compared to the observed T_B, using L_e calculated from different measurements and conversion coefficients. Table 3 and Table 4 list the T_B simulations. Table 5 summarizes the mean bias (MB), mean absolute error (MAE) and root-mean squared error (RMSE) of the predicted T_B.

The observed T_B at 19 and 37 GHz is 252 K and 233 K on February 22, and 248 K and 231 K on February 23. Using OSU stereological measurements and β_M of 0.75, MEMLS predicts the observed T_B with a MB of 0.05 K and an RMSE of 2.41 K. An error value of 2.41 K is not far from the precision of the radiometer T_B measurements (~2 K). The optimized β_O is 0.73, which is very close to 0.75. This optimization slightly reduced the RMSE from 2.41 K to 2.39 K, but increased the MB from 0.05 K to 0.55 K, which implies that the improvement from optimization is not significant. Therefore, it can be concluded that, the conventional β_M of 0.75 works for our snowpits, and the

493 stereological measurements can be used to accurately estimate T_B. For the February 22
494 snowpit, MEMLS T_B accurately estimated both frequencies with an error of -0.3 K and
495 0.8 K at 19 and 37 GHz, respectively. However, for the February 23 snowpit, T_B at 19
496 GHz is overestimated by 3.2 K and T_B at 37 GHz is underestimated by 3.5 K.
497 According to the stronger penetration ability of the low frequency and the fact that T_B
498 decreases with an increase of L_e, we would expect a slightly smaller L_e at the surface
499 layers and a slightly larger L_e at the bottom layers to closely match the observed T_B.

500 From Figure 9, the T_B bias using WSL L_e is larger for both snowpits at 19 GHz;
501 therefore, its RMSE (3.71 K) is slightly larger than OSU (2.41 K). However, a RMSE
502 of 3.71 K is still quite acceptable. An optimized β_O for the WSL stereological
503 measurements is 0.72. It reduced the MB from -1.40 K to 0.57 K, the MAE from 3.30 K
504 to 2.78 K, and the RMSE from 3.71 K to 3.23 K.

505 Using S_i measurements from NIR camera, the RMSE based on β_M is 6.52 K, and
506 the ME is -5.2 K. As can be seen in Figure 7, a large difference between the simulation
507 and the observation is from the February 23 snowpit, where T_B at 19 and 37 GHz was
508 underestimated by 10.9 K and 6.0 K, respectively. The error for the February 22
509 snowpit is only -3.9 K and 0.0 K on two frequencies, respectively. It shows clearly that
510 the much larger L_e derived from NIR photography for the bottom layers on February 23
511 contains some errors. An optimized β_O of 0.68 can reduce the RMSE from 6.52 K to
512 3.76 K and MB from -5.2 K to 0.0 K, but it degraded the accuracy at 37 GHz on
513 February 22. This optimized β was influenced by a few poor microstructure
514 measurements; thus, its value as a reference is reduced.

515 When L_e was converted from D_g measured by hand lens, the Durand's
516 conversion coefficients result in an overestimation of 8.08 K in average. T_B at both
517 frequencies and for both snowpits was overestimated. After optimization using an α_O of

1.16, it reduced the MB from 8.08 K to 1.85 K, MAE from 8.08 K to 3.40 K, and RMSE from 8.22 K to 4.35 K. The α_O of 1.16 is between the Durand et al. (2008) (α=1.0) and the Pan et al. (2016) (α=1.36) coefficients, and clearly represents a correction to systematic bias. After α was optimized, the biggest error comes from 19 GHz on February 23, which is 8 K overestimation. It indicates, albeit the systematic bias, the measured D_g at the bottom layers is still relatively underestimated. It agrees with the comparison with other measurement tools in Figure 8(b).

Overall, all the snow microstructure measurements, including S/V from the stereology, S_i from NIR photography and D_g from hand lens, give an RMSE below 9 K for T_B simulation without optimizing the L_e conversion coefficients. After optimization, it is possible to achieve an RMSE below 5 K using all measurements.

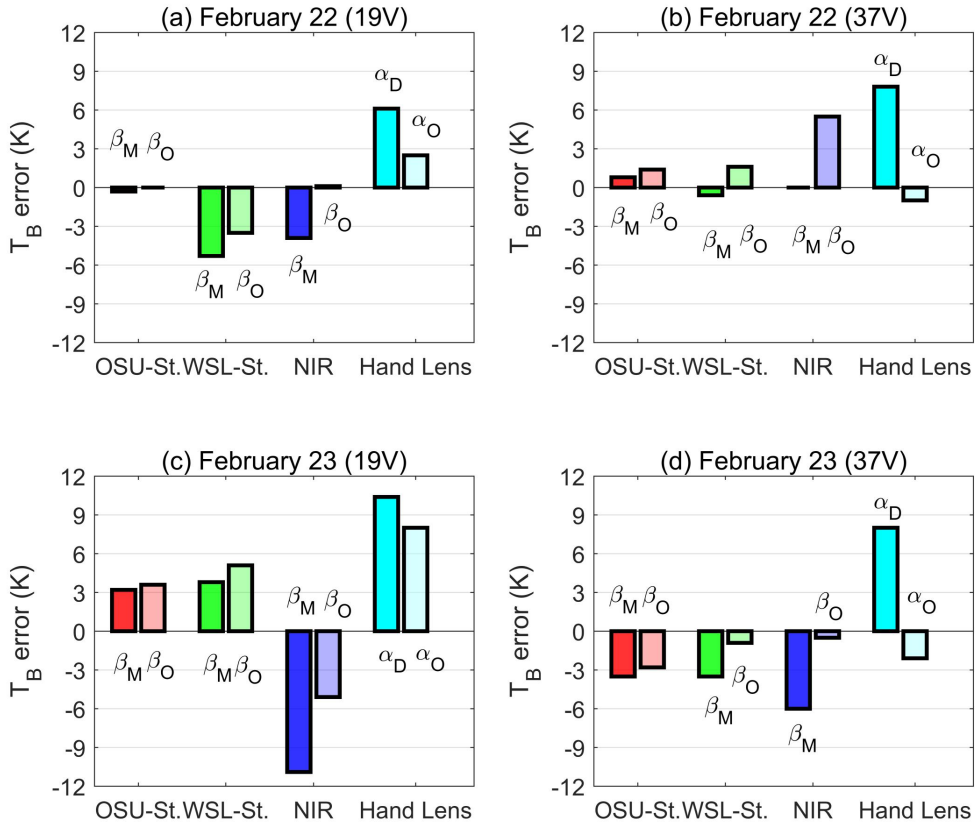

Figure 9. Error of predicted T_B by MEMLS using L_e from different methods: (a) 19 GHz on February 22, (b) 37 GHz on February 22, (c) 19 GHz on February 23, (d) 37

GHz on February 23. In each subplot, from left to right, L_e is from: OSU stereology using β_M and β_O, WSL stereology using β_M and β_O, NIR photography using β_M and β_O, hand lens using α_D and α_O.

Table 3. Comparison of the measured and the MEMLS-predicted T_B using stereology, NIR camera and hand lens measurements, when L_e was converted by conventional conversion coefficients.

T_B (K)	Scaling Factor	February 22		February 23	
		19 GHz	37 GHz	19 GHz	37 GHz
Observed T_B	-	252	233	248	231
Stereology-OSU	β_M=0.75	251.7	233.8	251.2	227.5
Stereology-WSL	β_M=0.75	246.7	232.4	251.8	227.5
NIR	β_M=0.75	248.1	233.0	237.1	225.0
Hand Lens	α_D=1.0	258.1	240.8	258.4	239.0

Table 4. Comparison of the measured and the MEMLS-predicted T_B, when L_e was converted by optimized conversion coefficients.

T_B (K)	Scaling Factor	February 22		February 23	
		19 GHz	37 GHz	19 GHz	37 GHz
Observed T_B	-	252	233	248	231
Stereology-OSU	B_O=0.73	252.0	234.4	251.6	228.2
Stereology-WSL	β_O=0.72	248.5	234.6	253.1	230.1
NIR	β_O=0.68	252.1	238.5	242.9	230.5
Hand Lens	α_O=1.16	254.5	232.0	256.0	228.9

Table 5. Error Statistics of the MEMLS-predicted T_B using different snow microstructure measurements and L_e conversion coefficients.

Measurements	Scaling Factor	Mean Bias, MB (K)	Mean Absolute Error, MAE (K)	Root Mean Squared Error, RMSE (K)
Stereology-OSU	β_M=0.75	0.05	1.95	2.41
	B_O=0.73	**0.55**	**1.95**	**2.39**
Stereology-WSL	β_M=0.75	-1.40	3.30	3.71
	β_O=0.72	**0.57**	**2.78**	**3.23**
NIR	β_M=0.75	-5.20	5.20	6.52
	β_O=0.68	**0.00**	**2.80**	**3.76**
Hand Lens	α_D=1.0	8.08	8.08	8.22
	α_O=1.16	**1.85**	**3.40**	**4.35**

6. Discussions

6.1 Influence of soil parameters

In this section, we evaluated the influences of the unmeasured volumetric soil water content and soil roughness to errors of the predicted T_B. The range of soil parameters used for simulation is 0-30% unfrozen volumetric soil water content (m_{vu}) and 0-2 cm surface root-mean-squared (rms) height. Figure 10 shows the sensitivity of T_B error at two frequencies for both snowpits, when L_e is calculated using OSU stereological measurements and β_M. In general, it shows the influence of both soil parameters to T_B at 37 GHz is minor. This is expected because the snow is very deep. However, T_B at 19 GHz does remain some sensitivity to the soil parameters.

The second question needs to be addressed is, did the soil parameter values impose a seemingly better performance using the OSU stereological measurements than other measurements? To answer this question, Figure 11 shows the MAE at 19 GHz using different L_e as a function of soil parameters. In Figure 11(a)-(b), the conventional conversion coefficients were used. Clearly, it shows MAE varies with the soil parameter values. However, in a m_{vu} range of 0-25% and soil roughness range of 0-2 cm, the MAEs using OSU stereological measurements are always the smallest. In Figure 11(c)-(d) where the optimized conversion coefficients were used, the MAE using OSU serological measurements is no longer always the smallest, but still less than at least two other types. Therefore, we can conclude that the highest T_B simulation performance from the utilization of stereological *S/V* is unaffected by soil parameter inputs and snow microstructure conversion coefficients.

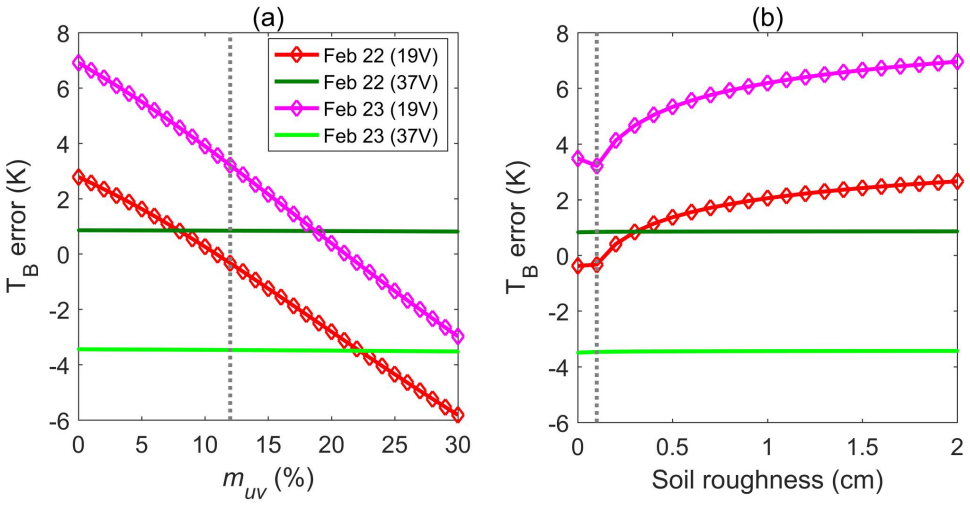

570

571 Figure 10. Error of the MEMLS predicted T_B as a function to unfrozen volumetric soil
572 water content (m_{vu}) (a) and soil roughness (b). The vertical gray dash lines represent the
573 12% m_{vu} and 0.1 cm roughness used for simulations in Section 5.2.

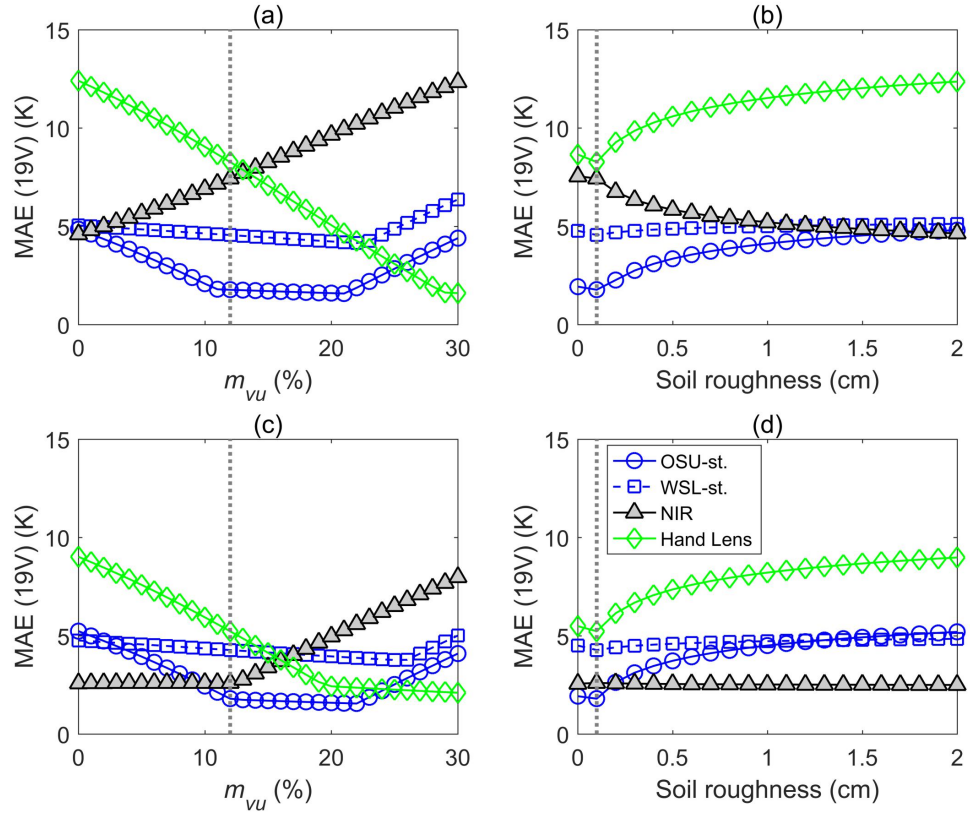

574

575 Figure 11. Sensitivity of MAE of the predicted T_B at 19 GHz to unfrozen volumetric
576 soil water content (m_{vu}) and soil roughness based on different microstructure
577 measurements: (a)-(b) used the conventional coefficients, (c)-(d) used the optimized
578 coefficients. st. represents stereology.

6.2 Influence of recrystallization to stereology

In this study, we observed the influence of recrystallization of casting agent on the stereological photo. The recrystallization leaves white spots on the sample sections, which covers or blurs the snow microstructure expected to be observed. Affected by the photo quality, the automatic segmentation by computer becomes unreliable. This is the most important reason why we only extracted S/V and S_i instead of the full ACF.

7. Conclusions

In this paper, an in-situ snow experiment was conducted at Steamboat Springs in Colorado mountain, US. The repeatability of stereological measurements was confirmed by comparing the estimates from two research groups based on seven samples from two deep snowpits, which contain both depth hoar and small facets/rounds. Later, the efficacy of the stereological measurements to predict the passive microwave T_B was evaluated. Results showed that the stereological measurement can be utilized to drive the Microwave Emission Model of Layered Snowpacks (MEMLS), a widely-used multi-layer snow radiative transfer model. MEMLS requires the exponential correlation length (L_e), whereas the stereology provides the surface to volume ratio (S/V). While the relationship between S/V and correlation length (L_c) is theoretical, an empirical fitting parameter is needed to further convert L_c into L_e. In this paper, we found the conversion coefficient β_M of 0.75 from the previous literature is usable for deep alpine snow in Colorado. It gives a RMSE of 2.41 and 3.71 K using the stereological measurements from the OSU and WSL research groups, respectively. This result highlights the utility of stereology to validate some more rapid SSA measurement tools in the context of microwave radiative transfer modelling.

The T_B modelling performance based on the stereological measurements was also compared with that based on NIR camera and hand lens measurements. The NIR

604 camera measures the snow specific surface area per ice volume (S_i), and the hand lens
605 provides the geometric grain size (D_g); they can also be used to drive MEMLS. Results
606 showed that, using the conversion coefficients from previous literatures without
607 optimization, the T_B RMSE is below 9 K in all cases. It can be reduced to below 5 K
608 after optimization; however, only the optimization for hand lens measured D_g represents
609 a correction for a systematic bias.

610 When snow is composed of different size ice grains and grain bonds, the snow
611 specific surface area (SSA) is a general parameter that represents the total surface area
612 of all components within a unit volume. Recent studies have shown that besides SSA, a
613 second-order microstructure parameter to represent the grain size distribution is
614 important for determining the snow ACF (Krol & Löwe, 2016) and the microwave
615 volume scattering (Chang et al., 2016). Such parameter can be the curvature length from
616 the snow sample measurement (Krol & Löwe, 2016), or the stickiness in DMRT models
617 (Picard et al., 2013) in the RT model configuration level. Therefore, we look forward to
618 more high-quality stereological or micro-CT measurements to answer these open
619 questions. On the other hand, although the D_g measurement has some degree of
620 subjective nature, its repeatability and objectiveness can be improved by postprocessing
621 the photo of a large number of crystals over a ruled card. Using this protocol, it is
622 possible to provide a grain size distribution to enrich the snow microstructure
623 description using fast SSA measurements in field.

624 **Acknowledgements:** This work was supported by the NASA Terrestrial Hydrology
625 Program under Grant no. NNX09AM10G and the Strategic Priority Research Program
626 of Chinese Academy of Sciences under Grant no. XDA20100300. The authors would
627 like to gratefully thank Ian McCubbin and Dr. Gannet Hallar for hosting us at Storm
628 Peak Laboratory, Ty Atkins for his invaluable assistance with the radiometer, and Dan
629 Berisford and Jennifer Petrzelka for their help in the snowpits. We would like to thank
630 Abiyu Getahun for his work on the stereological processing.

631

632 **References:**

633 Avanzi, Francesco, Giacomo Petrucci, Margret Matzl, Martin Schneebeli, and Carlo De
634 Michele. 2017. “Early formation of preferential flow in a homogeneous snowpack
635 observed by micro-CT.” *Water Resource Research* 53(5): 3713-3729. doi:
636 10.1002/2016WR019502.

637 Boyarskii, Dmitriy A., and Vasiliy V. Tikhonov. 2000. “The Influence of Stratigraphy
638 on Microwave Radiation from Natural Snow Cover.” *Journal of electromagnetic*
639 *waves and applications* 14(9): 1265–1285. doi:10.1163/156939300X01201.

640 Brucker, Ludovic., Ghislain Picard, Laurent Arnaud, Jean-Marc Barnola, Martin
641 Schneebeli, Hélène Brunjail, Eric Lefebvre,Michel Fily. 2011. “Modeling Time
642 Series of Microwave Brightness Temperature at Dome C, Antarctica, using
643 Vertically Resolved Snow Temperature and Microstructure Measurements.”
644 *Journal of Glaciology* 57(201): 171–182. doi: 10.3189/002214311795306736.

645 Chang, Alfred T., James L. Foster, Dorothy K.Hall. 1987. “Nimbus-7 SMMR Derived
646 Monthly Global Snow Cover and Snow Depth.” *Annals of Glaciology* 9: 39–44.
647 doi:10.3189/S0260305500200736.

648 Chang, Wenmo, Kunghau Ding, Leung Tsang, and Xiaolan Xu. 2016. “Microwave
649 Scattering and Medium Characterization for Terrestrial Snow With QCA–Mie and
650 Bicontinuous Models: Comparison Studies.” *IEEE Transactions on Geoscience*
651 *and Remote Sensing* 54(6): 3637–3648. doi: 10.1109/TGRS.2016.2522438.

652 Colbeck, Samuel C. 1991. “The Layered Character of Snow Covers.” *Reviews of*
653 *Geophysics* 29(1): 81-96. doi:10.1029/90RG02351.

654 Davis, Robert E., and Jeff Dozier. 1989. “Stereological Characterization of Dry Alpine
655 Snow for Microwave Remote Sensing.” *Advances in Space Research* 9(1): 245–
656 251. doi:10.1016/0273-1177(89)90492-4.

657 Debye, P., H. R. Anderson Jr., and H. Brumberger. 1957. “Scattering by an
658 Inhomogeneous Solid. II. the Correlation Function and Its Application.” *Journal of*
659 *Applied Physics* 28(6), 679–683. doi:10.1063/1.1722830.

660 Derksen, Chris, Juha Lemmetyinen, Joshua King, Stephane Belair, C. Garnaud, M.
661 Lapointe, Yves Crevier, G. Burbidge, Paul R. Siqueira. 2019. “A Dual-Frequency

662 Ku-band Radar Mission Concept for Seasonal Snow." *2019 IEEE International*
663 *Geoscience and Remote Sensing Symposium (IGARSS 2019)*: 5742-5744.
664 Yokohama, Japan, Jul. 28-Aug. 02, 2019. doi: 10.1109/IGARSS.2019.8898030.

665 Hall, Dorothy K., Alfred T. Chang, and James L. Foster. 1986. "Detection of the Depth-
666 hoar Layer in the Snow-pack of the Arctic Coastal Plain of Alaska, USA, Using
667 Satellite Data." *Journal of Glaciology* 32(110): 87–94.

668 Durand, Michael, Edward J Kim, and Steven A Margulis. 2008. "Quantifying
669 Uncertainty in Modeling Snow Microwave Radiance for a Mountain Snowpack at
670 the Point-Scale, Including Stratigraphic Effects." *IEEE Transactions on*
671 *Geoscience and Remote Sensing* 46(6): 1753–1767.
672 doi:10.1109/TGRS.2008.916221.

673 Durand, Michael, Edward J. Kim, Steven A. Margulis, and Noah P. Molotch. 2011. "A
674 first-order Characterization of Errors from Neglecting Stratigraphy in Forward and
675 Inverse Passive Microwave Modeling of Snow." *IEEE Geoscience and Remote*
676 *Sensing Letters* 8(4): 730-734. doi:10.1109/LGRS.2011.2105243.

677 Ebner, Pirmin Philipp, Martin Schneebeli, and Aldo Steinfeld. 2015. "Tomography-
678 Based Monitoring of Isothermal Snow Metamorphism under Advective
679 Conditions." *The Cryosphere* 9(4): 1363–1371. doi:10.5194/tc-9-1363-2015.

680 Elder, Kelly, Don Cline, Glen E. Liston, and Richard Armstrong. 2009. "NASA Cold
681 Land Processes Experiment (CLPX 2002/03): Field Measurements of Snowpack
682 Properties and Soil Moisture." *Journal of Hydrometeorology* 10 (1): 320–329.
683 doi:10.1175/2008JHM877.1.

684 Eppanapelli, Lavan Kumar, Forsberg, Fredrik Forsberg, Johan Casselgren, and Henrik
685 Lycksam. 2019. "3D Analysis of Deformation and Porosity of Dry Natural Snow
686 during Compaction." *Materials* 12(6): 850. doi: 10.3390/ma12060850.

687 Fierz, Charles, Richard L. Armstrong, Yves Durand, Pierre Etchevers, Ethan Greene,
688 David M. McClung, Kouichi Nishimura, Pramod K. Satyawali, and Sergey A.
689 Sokratov. 2009. The International Classification for Seasonal Snow on the Ground.
690 IHP–VII, Technical Documents in Hydrology, No 83; IACS Contribution No 1, 80,
691 Paris: International Hydrological Programme (IHP) of the United Nations
692 Educational, Scientific and Cultural Organization (UNESCO).

693 Gallet, Jean-Charles, Florent Domine, Charles S. Zender, and Ghislain Picard. 2009.
694 “Measurement of the Specific Surface Area of Snow Using Infrared Reflectance in
695 an Integrating Sphere at 1310 and 1550 nm.” *The Cryosphere* 3: 167–182.
696 doi:10.5194/tc-3-167-2009.

697 Gergely, Mathias, Fabian Wolfsperger, and Martin Schneebeli. 2014. “Simulation and
698 Validation of the InfraSnow: An Instrument to Measure Snow Optically Equivalent
699 Grain Size.” *IEEE Transactions on Geoscience and Remote Sensing* 52(7): 4236–
700 4247. doi:10.1109/TGRS.2013.2280502.

701 Haass-Koffler, Carolina L., Mohammad Naeemuddin, and Selena E. Bartlett. 2012. “An
702 Analytical Tool that Quantifies Cellular Morphology Changes from Three-
703 dimensional Fluorescence Images”. *Jove-Journal of Visualized Experiments* 66:
704 e4233. doi: 10.3791/4233.

705 Hagenmuller, Pascal, Margret Matzl, Guillaume Chambon, and Martin Schneebeli.
706 2016. “Sensitivity of Snow Density and Specific Surface Area Measured by
707 Microtomography to Different Image Processing Algorithms.” *The Cryosphere* 10:
708 1039–1054. doi:10.5194/tc-10-1039-2016.

709 Ishimoto, Hiroshi, Satoru Adachi, Satoru Yamaguchi, Tomonori Tanikawa, Teruo Aoki,
710 and Kazuhiko Masuda. 2018. “Snow Particles Extracted from X-ray Computed
711 Microtomography Imagery and Their Single-scattering Properties.” *Journal of*
712 *Quantitative Spectroscopy & Radiative Transfer* 209: 113-128. doi:
713 10.1016/j.jqsrt.2018.01.021.

714 Kim, Edward. 2009. “The Airborne Earth Science Microwave Imaging Radiometer
715 (AESMIR)-NASA's new passive microwave airborne imager” *2009 IEEE Sensors*,
716 Christchurch, New Zealand, 25-28 Oct. 2009: 1725–1728. doi:
717 10.1109/ICSENS.2009.5398492.

718 Kelly, Richard. 2009. “The AMSR-E snow depth algorithm: description and initial
719 results.” *Journal of the Remote Sensing Society of Japan* 29(1), 307-317.

720 Krol, Quirine, and Henning Löwe. 2016. “Relating Optical and Microwave Grain
721 Metrics of Snow: The relevance of Grain Shape.” *The Cryosphere* 10: 2847–2863.
722 doi: 10.5194/tc-10-2847-2016.

Langlois, Alexandre, Alain Royer, Benoit Montpetit, Ghislain Picard, Ludovic Brucker, Laurent Arnaud, Patrick Harveycollard, Michel Fily, and Kalifa Goïta. 2010. "On the Relationship between Snow Grain Morphology and In-Situ near Infrared Calibrated Reflectance Photographs." *Cold Regions Science and Technology* 61(1): 34–42. doi:10.1016/j.coldregions.2010.01.004.

Leinss, Silvan, Henning Lowe, Martin Proksch, Juha Lemmetyinen, Andreas Wiesmann, and Irena Hajnsek. 2016. "Anisotropy of Seasonal Snow Measured by Polarimetric Phase Differences in Radar Time Series." *The Cryosphere* 10 (4): 1771 – 1797. doi:10.5194/tc-10-1771-2016.

Lemmetyinen, Juha, Anna Kontu, Jouni Pulliainen, Juho Vehviläinen, Kimmo Rautiainen, Andreas Wiesmann, Christian Mätzler, Charles Werner, Helmut Rott, Thomas Nagler, Martin Schneebeli, Martin Proksch, Dirk Schüttemeyer, Michael Kern, Malcolm Davidson. 2016. "Nordic Snow Radar Experiment."*Geoscientific Instrumentation, Methods and Data Systems* 5(2): 403–415. doi:10.5194/gi-5-403-2016.

Löwe, Henning, and Picard, G. 2015. "Microwave Scattering Coefficient of Snow in MEMLS and DMRT-ML Revisited: the Relevance of Sticky Hard Spheres and Tomography-based Estimates of Stickiness." *The Cryosphere* 9(6), 2101–2117. doi: 10.5194/tc-9-2101-2015.

Malinka, Aleksey V. 2014. "Light Scattering in Porous Materials: Geometrical Optics and Stereological Approach." *Journal of Quantitative spectroscopy and radiative transfer* 141: 14 – 23. doi:10.1016/j.jqsrt.2014.02.022.

Wiese, Mareike, and Martin Schneebeli. 2017. "Snowbreeder 5: A Micro-CT Device For Measuring the Snow-microstructure Evolution Under the Simultaneous Influence of A Temperature Gradient And Compaction." *Journal of Glaciology* 63(238): 355-360. doi: 10.1017/jog.2016.143.

Matzl, Margret, and Martin Schneebeli. 2006. "Measuring Specific Surface Area of Snow by Near-Infrared Photography." *Journal of Glaciology* 52(179): 558–564. doi:10.3189/172756506781828412.

Matzl, Margret, and Martin Schneebeli. 2010. "Stereological Measurement of the Specific Surface Area of Seasonal Snow Types: Comparison to Other Methods,

754 and Implications for mm-Scale Vertical Profiling." *Cold Regions Science and*
755 *Technology* 64(1): 1–8. doi:10.1016/j.coldregions.2010.06.006.

756 Mätzler, Christian. 1987. "Applications of the Interaction of Microwaves with the
757 Natural Snow Cover." *Remote Sensing Reviews* 2 (2): 259–387.
758 doi:10.1080/02757258709532086.

759 Mätzler, Christian. 1997. "Autocorrelation Functions of Granular Media with Free
760 Arrangement of Spheres, Spherical Shells or Ellipsoids." *Journal of Applied*
761 *Physics* 81(3): 1509–1517. doi:10.1063/1.363916.

762 Mätzler, Christian. 1998. "Improved Bom Approximation for Scattering of Radiation in
763 a Granular Medium." *Journal of Applied Physics* 83(11): 6111–6117. doi:
764 10.1063/1.367496.

765 Mätzler, Christian, and Andreas Wiesmann, A. 1999. "Extension of the Microwave
766 Emission Model of Layered Snowpacks to Coarse-grained Snow." *Remote Sensing*
767 *of Environment* 70(3): 317–325.doi: 10.1016/S0034-4257(99)00047-4.

768 Mätzler, Christian. 2002. "Relation between Grain-Size and Correlation Length of
769 Snow." *Journal of Glaciology* 48(162): 461–466.
770 doi:10.3189/172756502781831287.

771 Wegmüller, Urs, and Christian Mätzler. 1999. "Rough Bare Soil Reflectivity Model."
772 *IEEE Transactions on Geoscience and Remote Sensing* 37(3): 1391–1395.doi:
773 10.1109/36.763303.

774 Montpetit, Benoit, Alain Royer, Alexandre Langlois, Patrick Cliche, Alexandre Roy, N.
775 Champollion, Ghislain Picard, Florent Domine, and R. Obbard. 2012. "New
776 Shortwave Infrared Albedo Measurements for Snow Specific Surface Area
777 Retrieval." *Journal of Glaciology*, 58(211): 941–952. doi:10.3189/2012JoG11J248.

778 Montpetit, Benoit, Alain Royer, Alexandra Roy, Alexandra Langlois, and Chris
779 Derksen. 2013. "Snow Microwave Emission Modeling of Ice Lenses Within a
780 Snowpack Using the Microwave Emission Model for Layered Snowpacks." *IEEE*
781 *Transactions on Geoscience and Remote Sensing* 51(9): 4705–4717.
782 doi:10.1109/TGRS.2013.2250509.

783 Painter, Thomas H, Noah P Molotch, Maureen Cassidy, Mark Flanner, and Konrad
784 Steffen. 2007. "Contact Spectroscopy for Determination of Stratigraphy of Snow

785 Optical Grain Size." *Journal of Glaciology* 53(180): 121–127.
786 doi:10.3189/172756507781833947.

787 Pan, Jinmei, Michael Durand, Melody Sandells, Juha Lemmetyinen, Edward Kim, Jouni
788 Pulliainen, Anna Kontu, and Chris Derksen. 2016. "Differences Between the HUT
789 Snow Emission Model and MEMLS and Their Effects on Brightness Temperature
790 Simulation." *IEEE Transactions on Geoscience and Remote Sensing* 54(4): 2001–
791 2019. doi:10.1109/tgrs.2015.2493505.

792 Perla, Ron, Jeff Dozier, and Robert E. Davis. 1986. Preparation of Serial Sections in
793 Dry Snow Specimens. *Journal of Microscopy* 142(1): 111–114.doi:
794 10.1111/j.1365-2818.1986.tb02744.x.

795 Phoulady, Hady Ahmady, Dmitry Goldgof, Lawrence O. Hall, Kevin R. Nash, and Peter
796 R. Mouton. 2019. "Automatic Stereology of Mean Nuclear Size of Neurons Using
797 An Active Contour Framework." *Journal of Chemical Neuroanatomy* 96: 110-115.
798 doi: 10.1016/j.jchemneu.2018.12.012.

799 Picard,Ghislain, Ludovic Brucker, Alexandre Roy, Florent Dupont, Michel Fily, Alain
800 Royer, and C Harlow. 2013. "Simulation of the Microwave Emission of Multi-
801 layered Snowpacks Using the Dense Media Radiative Transfer Theory: the
802 DMRT-ML model." *Geoscientific Model Development* 6(4): 1061–1078. doi:
803 10.5194/gmd-6-1061-2013.

804 Pinzer, Bernd R., and Martin Schneebeli. 2009. "Snow Metamorphism under
805 Alternating Temperature Gradients: Morphology and Recrystallization in Surface
806 Snow." *Geophysical Research Letters* 36(2): 1–4. doi:10.1029/2009GL039618.

807 Pulliainen, Jouni. 2006. "Mapping of Snow Water Equivalent and Snow Depth in
808 Boreal and Sub-Arctic Zones by Assimilating Space-Borne Microwave
809 Radiometer Data and Ground-Based Observations." *Remote Sensing of*
810 *Environment* 101(2): 257–269. doi:10.1016/j.rse.2006.01.002.

811 Proksch, Martin, Henning Lowe, and Martin Schneebeli. 2015a. "Density, Specific
812 Surface Area, and Correlation Length of Snow Measured by High-resolution
813 Penetrometry." *Journal of Geophysical Research* 120(2): 346–362.
814 doi:10.1002/(ISSN)2169-9011.

Proksch, Martin, Christian Mätzler, Andreas Wiesmann, Juha Lemmetyinen, M Schwank, Henning Löwe, and Martin Schneebeli. 2015b. "MEMLS3&a: Microwave Emission Model of Layered Snowpacks Adapted to Include Backscattering." *Geoscientific Model Development* 8(8): 2611–2626. doi:10.5194/gmd-8-2611-2015.

Reber, B., Christian Mätzler, and E. Schanda. 1987. "Microwave Signatures of Snow Crusts Modelling and Measurements." *International Journal of Remote Sensing* 8 (11): 1649–1665. doi:10.1080/01431168708954805.

Riche, Fabiene, Martin Schneebeli, and Stefan A Tschanz. 2012. "Design-Based Stereology to Quantify Structural Properties of Artificial and Natural Snow Using Thin Sections." *Cold Regions Science and Technology* 79–80: 67–74. doi:10.1016/j.coldregions.2012.03.008.

Rutter, Nick, Mel Sandells, Chris Derksen, Peter Toose, Alain Royer, Benoit Montpetit, Alex Langlois, Juha Lemmetyinen, and Jouni Pulliainen. 2014. "Snow Stratigraphic Heterogeneity within Ground-based Passive Microwave Radiometer Footprints: Implications for Emission Modeling." *Journal of Geophysical Research* 119(3): 550–565. doi:10.1002/2013JF003017.

Rutter, Nick, Melody J Sandells, Chris Derksen, Joshua King, Peter Toose, Leanne Wake, Tom Watts, et al. 2019. "Effect of Snow Microstructure Variability on Ku-Band Radar Snow Water Equivalent Retrievals." *Cryosphere* 13 (11): 3045–3059. doi:10.5194/tc-13-3045-2019.

Rott, Helmut, Donald W. Cline, Claude Duguay, Richard Essery, Pierre Etchevers, Irena Hajnsek, Michael Kern, Giovanni Macelloni, Eirik Malnes, Jouni Pulliainen, and Simon H. Yeuh. 2013. "CoReH2O, a Candidate ESA Earth Explorer Mission for Snow and Ice Observations." In *Proc. Earth Observation and Cryosphere Science Workshop*, ESA SP-712 (May 2013). Frascati, Italy, 13-16 November 2012.

Roy, Alexandre, Ghislain Picard, Alain Royer, Benoit Montpetit, Florent Dupont, Alexandre Langlois, Chris Derksen, and N. Champollion. 2013. "Brightness Temperature Simulations of the Canadian Seasonal Snowpack Driven by Measurements of the Snow Specific Surface Area." *IEEE Transactions on*

Geoscience and Remote Sensing 51(9): 4692–4704. doi:10.1109/TGRS.2012.2235842.

Sandells, Melody, Richard Essery, Nick Rutter, Leanne Wake, Leena Leppänen, and Juha Lemmetyinen. 2017. "Microstructure Representation of Snow in Coupled Snowpack and Microwave Emission Models." *Cryosphere* 11 (1): 229 – 246. doi:10.5194/tc-11-229-2017.

Shain, W., S. Kayali, D. Szarowski, M. Davis-Cox, H. Ancin, A. K. Bhattacharjya, B. Roysam, J. N. Turner. 1999. "Application and Quantitative Validation of Computer-automated Three-dimensional Counting of Cell Nuclei" *Microscopy and Microanalysis* 5(2): 106-119. doi: 10.1017/S1431927699000069.

Sturm, Matthew, Jon Holmgren, Max König, and Kim Morris. 1997. "The thermal conductivity of seasonal snow". *Journal of Glaciology* 43(143): 26-41. doi: 10.3189/s0022143000002781.

Takala, Matias, Kari Luojus, Jouni Pulliainen, Chris Derksen, Juha Lemmetyinen, Juha Petri Kärnä, Jarkko Koskinen, and Bojan Bojkov. 2011. "Estimating Northern Hemisphere Snow Water Equivalent for Climate Research through Assimilation of Space-Borne Radiometer Data and Ground-Based Measurements." *Remote Sensing of Environment* 115(12): 3517–3529. doi:10.1016/j.rse.2011.08.014.

Tedesco, Marco, and Parag S. Narvekar. 2010. "Assessment of the NASA AMSR-E SWE Product." *IEEE Journal of Selected Topics in Applied Earth Observations and Remote Sensing* 3(1): 141-159. doi:10.1109/JSTARS.2010.2040462.

Wiesmann, Andreas, Christian Mätzler, and Thomas Weise. 1998. "Radiometric and Structural Measurements of Snow Samples." *Radio Science* 33(2): 273–289. doi:10.1029/97RS02746.

Wiesmann, Andreas, and Christian Mätzler. 1999. "Microwave Emission Model of Layered Snowpacks." *Remote Sensing of Environment* 70(3): 307–316. doi:10.1016/S0034-4257(99)00046-2.

Wiscombe, Warren J., and Warren Stephen G. 1980. "A model for the Spectral Albedo of Snow. I: Pure Snow." *Journal of the Atmospheric Sciences* 37: 2312-2733. doi: 10.1175/1520-0469(1980)037<2712:AMFTSA>2.0.CO;2.

876 Xiong, Chuan, Jiancheng Shi, Lingmei Jiang, and Yurong Cui. 2016. “Global Mapping
877 of Snow Water Equivalent with The Water Cycle Observation Mission (WCOM).”
878 *2016 IEEE International Geoscience and Remote Sensing Symposium (IGARSS)*,
879 Beijing, China, Jul. 10-15 2016: 7396 – 7399. doi:
880 10.1109/IGARSS.2016.7730929.

881 Xiong, Chuan, Jiancheng Shi, Marco Brogioni, and Leung Tsang. 2012. “Microwave
882 Snow Backscattering Modeling Based on Two-Dimensional Snow Section Image
883 and Equivalent Grain Size.” 2012 *IEEE International Geoscience and Remote*
884 *Sensing Symposium (IGARSS)*, Munich, Germany, 12 November 2012: 150–153.
885 doi:10.1109/IGARSS.2012.6351615.

886 Zhang, Lixin, Jiancheng Shi, Zhongjun Zhang, and Kaiguang Zhao. 2003. “The
887 Estimation of Dielectric Constant of Frozen Soil-Water Mixture at Microwave
888 Bands.” Proceedings of 2003 *IEEE International Geoscience and Remote Sensing*
889 *Symposium (IGARSS)* (IEEE Cat. No.03CH37477), Toulouse, France, 21-25 July
890 2003 (4): 2903 – 2905. doi:10.1109/IGARSS.2003.1294626.

891 Zuanon, Nicolas. 2013. “IceCube, a Portable and Reliable Instruments for Snow
892 Specific Surface Area Measurement in the Field.” *Proceedings of International*
893 *Snow Science Workshop Grenoble*, Chamonix Mont-Blanc, France, 7-11 October
894 2013: 1021–1023.